




Multidimensional four-wave mixing signals detected by quantum squeezed light

Konstantin Dorfman^{a,1,2} , Shengshuai Liu^{a,1}, Yanbo Lou^{a,1}, Tianxiang Wei^a, Jietai Jing^{a,b,c,d,2}, Frank Schlawin^{e,f} , and Shaul Mukamel^{g,h} 

^aState Key Laboratory of Precision Spectroscopy, Joint Institute of Advanced Science and Technology, School of Physics and Electronic Science, East China Normal University, Shanghai 200062, China; ^bCAS Center for Excellence in Ultra-intense Laser Science, Shanghai 201800, China; ^cDepartment of Physics, Zhejiang University, Hangzhou 310027, China; ^dCollaborative Innovation Center of Extreme Optics, Shanxi University, Taiyuan 030006, China; ^eMax Planck Institute for the Structure and Dynamics of Matter, 22761 Hamburg, Germany; ^fThe Hamburg Centre for Ultrafast Imaging, Hamburg D-22761, Germany; ^gChemistry Department, University of California, Irvine, CA 92697-2025; and ^hPhysics and Astronomy Department, University of California, Irvine, CA 92697-2025

Edited by Gregory S. Engel, University of Chicago, Chicago, IL, and accepted by Editorial Board Member Peter J. Rossky July 3, 2021 (received for review March 23, 2021)

Four-wave mixing (FWM) of optical fields has been extensively used in quantum information processing, sensing, and memories. It also forms a basis for nonlinear spectroscopies such as transient grating, stimulated Raman, and photon echo where phase matching is used to select desired components of the third-order response of matter. Here we report an experimental study of the two-dimensional quantum noise intensity difference spectra of a pair of squeezed beams generated by FWM in hot Rb vapor. The measurement reveals details of the $\chi^{(3)}$ susceptibility dressed by the strong pump field which induces an AC Stark shift, with higher spectral resolution compared to classical measurements of probe and conjugate beam intensities. We demonstrate how quantum correlations of squeezed light can be utilized as a spectroscopic tool which unlike their classical counterparts are robust to external noise.

quantum spectroscopy | multidimensional spectroscopy | squeezed light

Quantum light and its statistics (1–13) provide powerful tools for the study of properties of matter that are hard to retrieve with classical light. Novel spectroscopic and sensing techniques based on quantum light sources (14) can reveal information about complex material systems that is not accessible by simply varying the frequencies or time delays of classical light pulses (15, 16). The state of quantum light provides most valuable control parameters. The matter response imprinted in the quantum light statistics can be retrieved by measuring higher-order correlation functions of the photon number. Spectroscopic measurements with entangled photons provide a unique observation window for the material response by accessing as well as controlling exciton distributions and transport processes (17), and the charge density in diffraction imaging (18, 19). Apart from their novel matter information, quantum light measurements have higher signal-to-noise ratio (20), and allow to shift optical measurements to desired frequency regimes where optical equipment is more readily available (21).

Here we focus on a class of quantum spectroscopy measurements of the multimode correlated squeezed light generated by four-wave mixing (FWM) (4, 22–27). Squeezed light can be broadly defined as a state of light whose quadrature amplitudes of the electric and magnetic fields are squeezed, that is, whose quantum uncertainty in one quadrature is smaller than that of a coherent state, typical for lasers. Fig. 1A shows the standard FWM setup used for squeezed light generation, which become a powerful spectroscopy tool. After an FWM process, the probe (blue line) and conjugate (yellow line) beams are multimode squeezed and they can be detected by, for example, a classical intensity measurement. Following the approach outlined in ref. 28, we have calculated the probe and conjugate transmitted intensities,

$$\langle \hat{N}_{pr} \rangle \simeq G \langle \hat{N}_0 \rangle, \quad \langle \hat{N}_c \rangle \simeq (G - 1) \langle \hat{N}_0 \rangle, \quad [1]$$

where $G(-\omega_{pr}, -\omega_c; 2\omega_{pu}) = \cosh^2[\chi^{(3)}(-\omega_{pr}, -\omega_c; 2\omega_{pu})]$ is the FWM gain governed by a third-order susceptibility $\chi^{(3)}$ dressed by the strong pump field (see *Materials and Methods*), and $\langle \hat{N}_0 \rangle = |\alpha|^2$ is the average photon number of the input probe beam. Rather than detecting classical field intensities, one can measure quantum fluctuations of the relative squeezing spectra defined by

$$S_N \equiv \frac{\text{Var}(\hat{N}_{pr} - \hat{N}_c)}{\langle \hat{N}_{pr} \rangle + \langle \hat{N}_c \rangle} = \frac{1}{2G - 1}, \quad [2]$$

which can be reduced to below the shot noise limit (SNL), providing a notable quantum advantage in weakly absorbing materials. To observe quantum squeezing of the probe and conjugate beams, we measure their intensity difference noise power spectrum and compare it with its corresponding SNL. The extent of quantum squeezing is given by the degree to which the intensity difference noise power is lower than SNL. As shown in Fig. 1A, the output probe and conjugate beams are sent to two silicon photodetectors (D_1 and D_2 , respectively). We can then

Significance

Quantum light and its statistics provide powerful tools for the study of properties of matter that are difficult to retrieve with classical light. Novel spectroscopic and sensing techniques based on quantum light sources can reveal information about complex material systems that is not accessible by varying the frequencies or time delays of classical light pulses. Here, based on a four-wave mixing process, we report an experimental study of the 2D quantum noise spectra of two-beam intensity difference squeezing. External noise erodes the resolution of classical measurements, while quantum signals remain intact. Our results pave the way for exploiting quantum correlations of squeezed light for spectroscopic applications.

Author contributions: K.D., J.J., F.S., and S.M. designed research; K.D., S.L., Y.L., T.W., and J.J. performed research; K.D. contributed new reagents/analytic tools; K.D. analyzed data; and K.D., S.L., Y.L., T.W., J.J., F.S., and S.M. wrote the paper.

The authors declare no competing interest.

This article is a PNAS Direct Submission. G.S.E. is a guest editor invited by the Editorial Board.

This open access article is distributed under [Creative Commons Attribution-NonCommercial-NoDerivatives License 4.0 \(CC BY-NC-ND\)](https://creativecommons.org/licenses/by-nc-nd/4.0/).

See [online](#) for related content such as Commentaries.

¹K.D., S.L., and Y.L. contributed equally to this work.

²To whom correspondence may be addressed. Email: dorfman@ips.ecnu.edu.cn or jtjing@phy.ecnu.edu.cn.

This article contains supporting information online at <https://www.pnas.org/lookup/suppl/doi:10.1073/pnas.2105601118/-DCSupplemental>.

Published August 13, 2021.

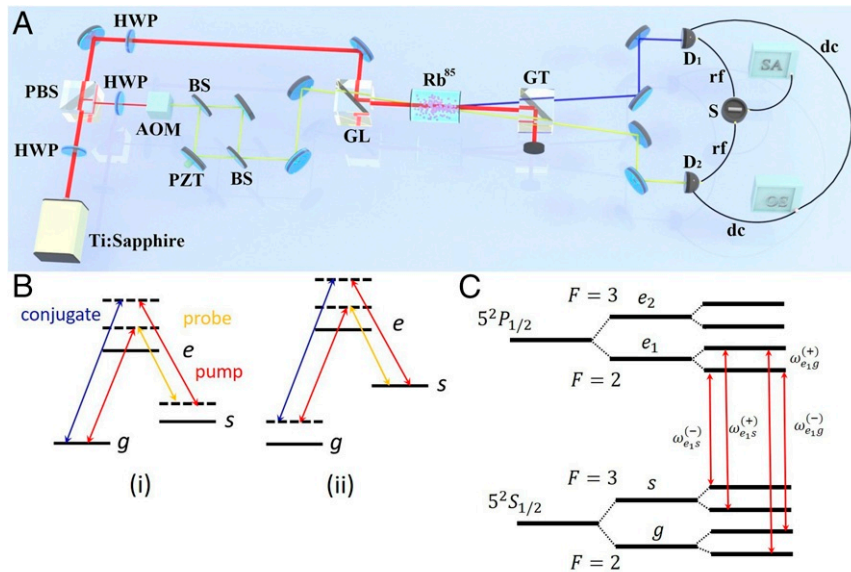


Fig. 1. (A) The experimental layout. A strong classical pump beam (red line) and a weak probe (yellow line) (in a coherent state with $|\alpha| \sim 600$ which corresponds to $10\text{-}\mu\text{W}$ power) are crossed in an ^{85}Rb vapor cell at a small angle. The probe beam is amplified, and a new conjugate beam (blue line) is generated on the other side of the vapor cell. The phase matching is given by $2k_{pu} = k_{pr} + k_c$, where subscripts indicate pump, probe, and conjugate beams. The probe and conjugate beam intensities can be either measured separately (classical measurement) or combined on an S to reveal the noise spectra of the intensity difference (Eq. 2) (quantum measurement). HWP, half-wave plate; PBS, polarization beam splitter; BS, beam splitter; AOM, acousto-optic modulator; PZT, piezoelectric transducer; GL, Glan–Laser polarizer; GT, Glan–Thompson polarizer; D1 (D2), photodetector; OS, oscilloscope; yellow lines, signal beam; blue lines, idler beam; red lines, pump beam. (B) Level scheme for the FWM process. Since the pump beam drives both electronic transitions $g \rightarrow e$ and $s \rightarrow e$, while the probe (conjugate) interacts only with $e \rightarrow g$, *i* indicates the case where initial state of the vapor is ground state g , while *ii* corresponds to the case when s is initially populated. (C) The ^{85}Rb -level scheme in the presence of the strong pump.

obtain the direct current (dc) and radio frequency (rf) components of the photocurrents. The rf components from the two ports are subtracted by using an rf subtractor (S) and then analyzed with a spectrum analyzer (SA). The subtracted result constitutes their intensity difference noise power spectrum. To obtain the corresponding SNL, we use a coherent beam with a power equal to the total power of the output beams. We then divide it into two beams with a 50:50 beam splitter and send the obtained beams into the two previously used photodetectors to get the noise power of the differential photocurrent, which gives the corresponding SNL. By scanning the pump and probe frequencies across several hundred megahertz, one can obtain a two-dimensional (2D) spectrum containing valuable matter information. While, in the standard FWM squeezed light generation scheme, the squeezing occurs between single modes at fixed frequencies, here the pump and probe frequencies scanned over the broad range ensure a multimode squeezing. While this measurement is not novel, but the spectroscopic advantage is certainly unique. By scanning the pump and probe pulse frequencies across several hundred megahertz, one obtains a 2D spectrum containing valuable matter information. In the standard FWM squeezed light generation scheme, the squeezing occurs between single modes at fixed frequencies; here, in contrast, the pump and probe frequencies scanned over the broad range ensure a multimode squeezing. A perturbative theoretical analysis provides a simple account of the squeezing measurements in SiV^- color centers in diamond (29) (see *SI Appendix*, section S1). Note that, in contrast with techniques where the quantum light sources are directed at the material to probe its response (14), here the generation of quantum light combined with quantum detection of squeezing serves as a probe of the nonlinear response of matter.

Results

Experimental Scheme. We consider an FWM process based on the double- Λ level scheme shown in Fig. 1B. Two lower hyperfine states g ($F = 2$) and s ($F = 3$) are separated by 3.035 GHz, while the upper states e_1 ($F = 3$) and e_2 ($F = 2$) are separated by 361.58 MHz. At vapor temperature 113°C , both g and s states are almost equally populated. The FWM may take place starting from either the g or s states as shown by level schemes *i* and *ii*, since the strong pump beam interacts with both $g \rightarrow e$ and $s \rightarrow e$ transitions. In diagram *i*, the pump first drives the $g \rightarrow e$ transition, while the probe drives the $e \rightarrow s$ transition. Another pump photon promotes the system via the $s \rightarrow e$ transition, while the conjugate beam generated by the FWM brings the system back to its ground state via $e \rightarrow g$ transition. The book-keeping of the field–matter interactions is shown in diagram *ia* in *SI Appendix*, Fig. S1. One can describe diagram *ii* similarly by exchanging states $g \leftrightarrow s$ and probing with conjugate beams. Due to the strong pump (180 mW), all four transitions, $g \rightarrow e_{1,2}$ and $s \rightarrow e_{1,2}$, show an AC Stark splitting which results in the transition frequency detunings $\omega_{e_j m}^{(\pm)} = \delta_{e_j m} / 2 \pm \Omega'_{e_j m}$, where $\Omega'_{e_j m} = \sqrt{\delta_{e_j m}^2 / 4 + \Omega_{e_j m}^2}$, $\delta_{e_j m} = \omega_{pu} - \omega_{e_j m}$ is the detuning and $\Omega_{e_j m} = \mu_{e_j m} \varepsilon_{pu}$, $j = 1, 2$, $m = g, s$ is a Rabi frequency corresponding to the pump field amplitude ε_{pu} for a given transition dipole moment $\mu_{e_j m}$ (Fig. 1C). The following two points should be noted. First, the pump should be strong enough to induce an AC Stark splitting, thus doubling the number of measured resonances. Peaks missed by classical intensity measurements clearly show up in the squeezing detection, thanks to the higher signal-to-noise ratio. Second, in the absence of losses, both intensity and squeezing measurements carry identical information associated with the FWM gain. This is no longer the case when optical losses exist. The squeezing measurement is robust to external

noise added to the pump and therefore to all the output fields of the FWM process. However, classical measurements become unstable and hard to interpret under these conditions.

Experimental Results. We start with a classical measurement of the transmission intensities of the probe and conjugate beams given by Eq. 1. In standard treatments of FWM-generated squeezed light fields, all transitions are kept off-resonant with respect to matter, and $\chi^{(3)}$ can be replaced by a frequency-independent prefactor. Here, in contrast, we are interested in resonant properties of the nonlinear response which can be measured through the probe or conjugate intensities. Fig. 2A demonstrates that, for a weak pump (100 mW), the 2D gain spectra (Eq. 1) displayed vs. one-photon detuning $\delta_1 = \omega_{pu} - \omega_{pu}^{(0)}$ with the reference frequency arbitrarily fixed by the experimental setup is $\omega_{pu}^{(0)} = 377109.2$ GHz and two-photon detuning $\delta_2 = \omega_{pu} - \omega_{pr} - \omega_{sg}$ shows a total of four peaks which can be described by $\omega_{pu} - \omega_{pr} = \omega_{e_qg}^{(\mu)} - \omega_{e_p s}^{(\nu)}$, $\mu, \nu = \pm, p, q = 1, 2$. Two central peaks denoted 2 and 3 correspond to the two-photon resonances corresponding to $\mu = -, \nu = +$ with $p = q = 1$ and $p = q = 2$, respectively. Two weaker side peaks denoted as 1 and 4 correspond to $\mu = \nu = -, p = q = 1$ and $\mu = \nu = +, p = q = 1$, respectively. A similar pattern is observed for the conjugate beam in Fig. 2B. The quantum squeezing signal S_N (Eq. 2) represents the relative noise corresponding to the degree of squeezing between the probe and conjugate fields. It is defined as a ratio of the relative intensity noise to the sum of the individual beams shot noise figures. S_N is depicted on a log scale $-10 \log(2G - 1)$ in Fig. 2C. The use of a log scale for quantum measurement (1) is natural since the noise spectra are normalized to unity for classical fields. Therefore, the noise of the quantum fields must be below one, which can be better visualized in a log scale. While the number and positions of peaks remain similar to the classical

measurement, their shapes and relative intensities are different. For instance, peaks 1 and 4, which are barely visible in the gain spectra, are well pronounced in the squeezing signal. Note that the noise spectra in Fig. 2C are not identical to the classical signals of Fig. 2A and B. To make a fair comparison, we used a logarithmic scale for the S_N measurement using classical gain from Fig. 2D, which is shown in SI Appendix, Fig. S3. It contains the same number of peaks as a nonlogarithmic classical probe gain in Fig. 2D, highlighting the difference between squeezed measurement (Eq. 2) and the classical gain measurements (Eq. 1), providing a different observation window onto the susceptibility $\tilde{\chi}^{(3)}$ composed of the terms given by Eq. 5 and derived in SI Appendix, section S1.

As the pump intensity is further increased to 180 mW, the AC Stark shift grows, and the four peaks described above are shifted accordingly, as seen in Fig. 2D and E. However, the squeezing spectra undergo more dramatic changes. In addition to the original four peaks 1 through 4, Fig. 2F contains four additional peaks (Table 1). This additional information is accessible only by a strong field and quantum squeezing detection, and is missed by classical detection. This arises since the quantum squeezing measurement is higher order in field-matter interactions and thus is not polluted by linear processes which may preclude the detection of weaker resonances. When optical losses are included, the signal-to-noise ratio of such higher-order correlation measurements is significantly increased.

To rationalize the experimental observations of Fig. 2, we developed a microscopic theoretical model for the $\tilde{\chi}^{(3)}$ susceptibilities, including the AC Stark shifts due to the strong pump. Here the matter response is governed by a $\tilde{\chi}^{(3)}$ susceptibility dressed by a strong pump field, which is different from the standard weak field susceptibility $\chi^{(3)}$. Details are presented in

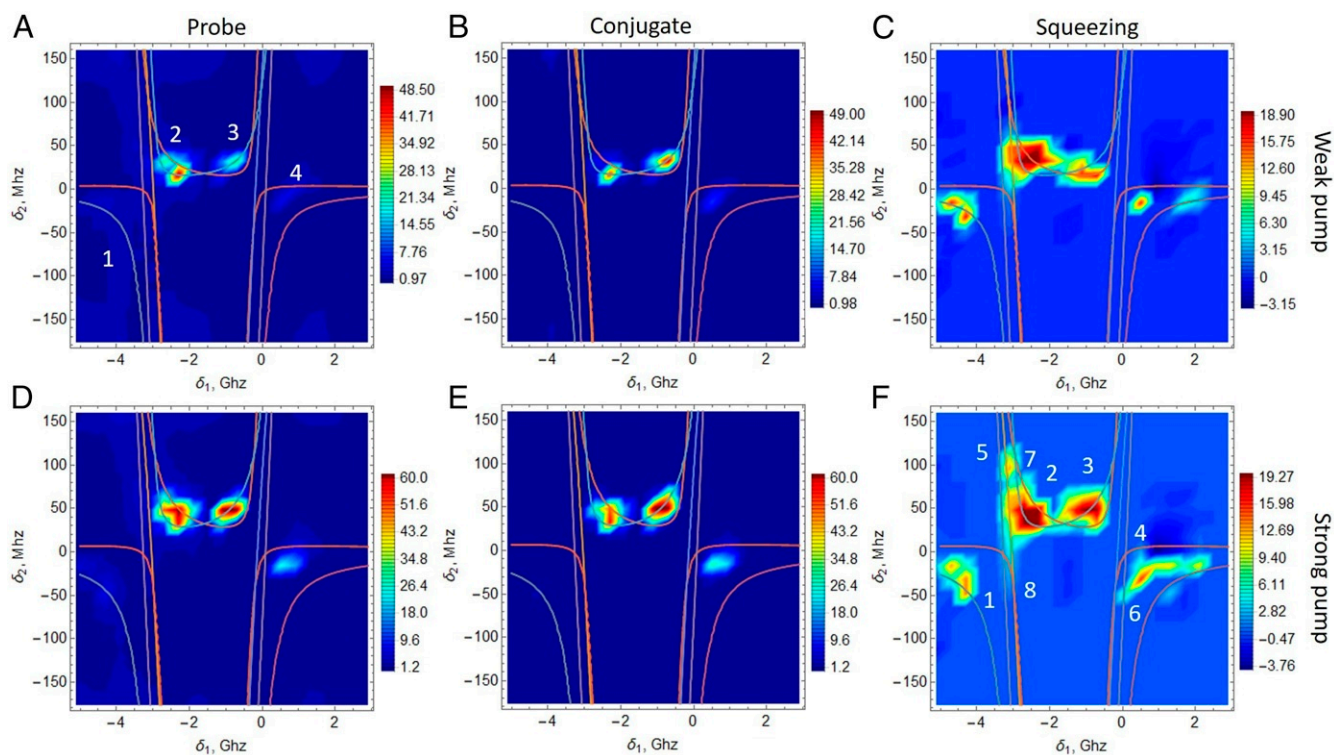


Fig. 2. Experimental 2D spectra of the classical and quantum signals. Eq. 3 displayed vs. the one-photon $-\delta_1 = \omega_{pu} - \omega_{pu}^{(0)}$ where $\omega_{pu}^{(0)} = 377,109.2$ GHz and two-photon $\delta_2 = \omega_{pu} - \omega_{pr} - \omega_{sg}$ detunings (A) probe and (B) conjugate photon numbers, and (C) squeezing Eq. 4, for the weak 100-mW pump. (D–F) Same as A–C but for a strong 180-mW pump. Color lines indicate positions of the AC Stark-shifted resonances calculated using Eq. 5.

Table 1. Resonant structure of the susceptibility in Eq. 5 depicted in Fig. 2 highlighting the sign of the AC Stark shifts

Peak no.	μ_g	ν_g	λ_g	μ_s	ν_s	p	q	Diagram
1	—	—	—	—	—	1	1	ii, iib
2	+	+	+	—	—	2	2	ii, iib
3	—	—	—	+	+	1	1	ia, ib
4	+	+	+	+	+	2	2	ia, ib
5	+	—	+	—	—	2	2	ii, iib
6	+	—	—	+	+	1	1	ia
7	+	+	+	—	—	1	1	ii, iib
8	—	+	+	—	—	2	2	ii

SI Appendix, section S2. We maintain a nonperturbative treatment of the strong classical pump, while retaining the lowest-order perturbation expansion in the probe and conjugate beams. Eq. 5 reveals the resonant pattern of the susceptibility. We include optical losses during the propagating through the material cell after the FWM process described by Eqs. 6 and 7. These losses occur when the strong pump field-driven transitions $s \rightarrow e_j$ ($g \rightarrow e_j$, $j = 1, 2$) undergo a spontaneous or stimulated emission with frequency matching the probe (conjugate) field. We thus obtain, for the classical measurement (28) (see *SI Appendix, section S3*),

$$\langle \hat{N}_{pr} \rangle \simeq \eta_{pr} G \langle \hat{N}_0 \rangle, \quad \langle \hat{N}_c \rangle \simeq \eta_c (G - 1) \langle \hat{N}_0 \rangle. \quad [3]$$

The corresponding noise figure is given by

$$S_N = 1 + \frac{2(G - 1)(G(\eta_{pr} - \eta_c)^2 - \eta_c^2)}{\eta_{pr} G + \eta_c (G - 1)}. \quad [4]$$

Fig. 3A shows the 2D spectra of the simulated probe gain for the strong 180-mW pump. All four peaks shown in Fig. 2D are repro-

duced with good agreement with experiment. The 1D segments of the spectra vs. single-photon detuning δ_1 for a given two-photon detuning $\delta_2 = -30, 0, \text{ and } 50$ MHz depicted by dashed white lines are displayed separately in Fig. 3B, C, and D, respectively, and show good agreement between theory and experiment (30). The corresponding squeezing measurement is shown in two dimensions in Fig. 3E together with 1D cross-sections depicted in Fig. 3F–H. All eight peaks are well reproduced by the theory. In addition, the quantum regime (negative noise spectra) shown in Fig. 3G indicates the correct magnitude of the noise figure in both quantum (squeezing) and classical regimes. To demonstrate the merits of quantum over classical detection, we added a random time modulation of the input probe beam intensity by utilizing a Mach–Zehnder interferometer as shown in Fig. 4. The red line shows the squeezing, while blue and yellow correspond to classical separate intensity measurements of the conjugate and probe fields, respectively. While the output fields intensity is proportional to the input intensities, the variance of the intensity difference is governed by the sum of variances of the individual classical fields, which is then governed by the sum of the probe and conjugate field intensities. Thus, the overall noise contribution from classical fields will add up. On the other hand, the variance of the photon number difference of the quantum fields is different due to nonzero covariance due to quantum correlations shared between the fields, which reduces the photon number difference below classical noise levels (23). The corresponding squeezing measurement is then governed only by the gain of the FWM. Therefore, the same noise reduction achieved by quantum measurement may not be reached by using classical measurements. This conclusion holds when squeezing is below the shot noise as shown in Fig. 4A (corresponding to the dark blue area in Fig. 2C) as well as in the opposite limit, when noise is above the shot noise level as seen in Fig. 4B. A similar effect was observed in entangled photon spectroscopy, where the spectroscopic information has been obtained in the presence of an external noise such as background

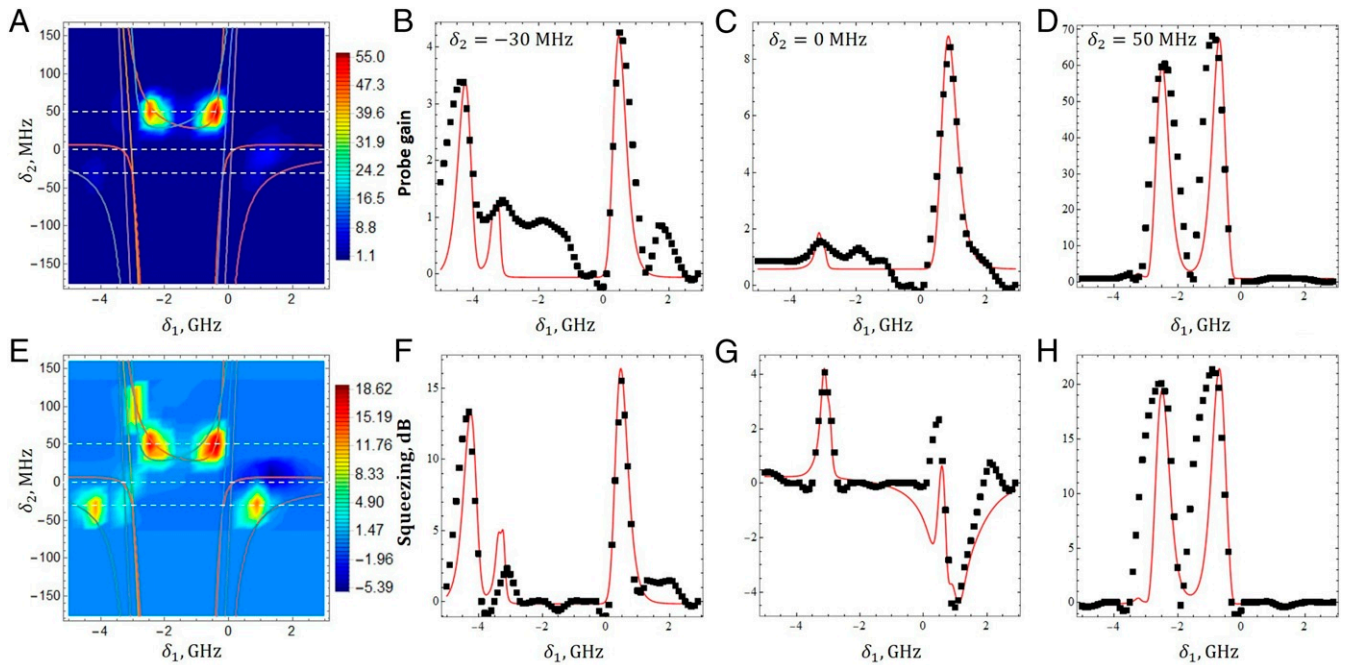


Fig. 3. Calculated 2D probe gain spectra Eq. 3 (A) with 1D slices (red line, theory; black dots, experiment) displayed vs. δ_1 evaluated at (B) $\delta_2 = -30$ MHz, (C) $\delta_2 = 0$ MHz, and (D) $\delta_2 = 50$ MHz. (E–H) Same as A–D but for the noise figure in Eq. 4. Rb gas parameters used in simulations are taken from ref. 28. The values of the coefficient of determination (R^2) defined in *SI Appendix, Eq. S22* in Fig. 3 B–E, G, and H are 0.41, 0.92, 0.72, 0.85, 0.58, and 0.51, respectively (see *SI Appendix, section S4*).

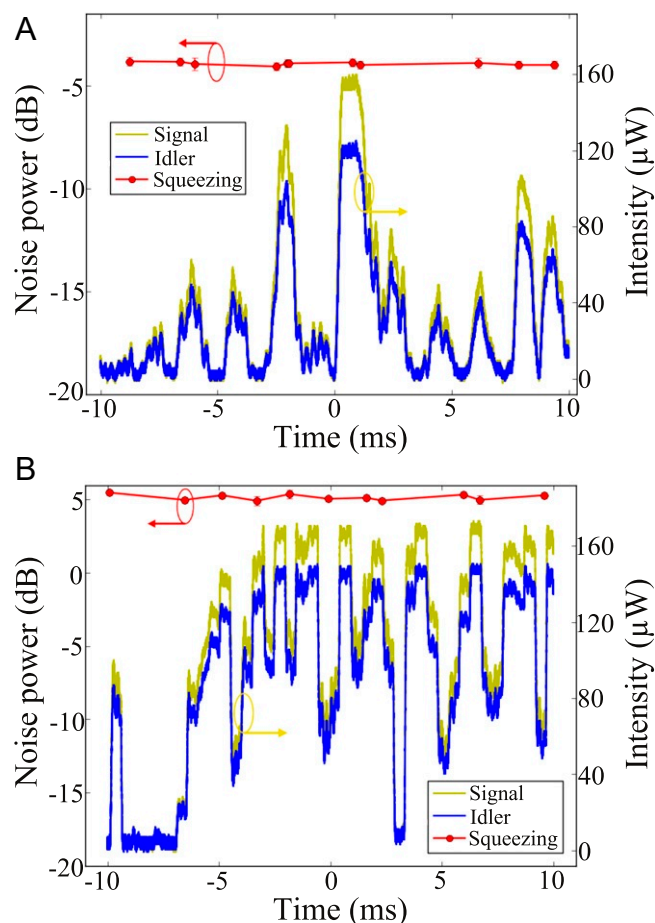


Fig. 4. (A) Experimental time evolution of the signals due to random time modulation of the input probe intensity. Output probe intensity Eq. 3 (yellow), conjugate (blue), and squeezing Eq. 4 (red) evaluated at $\delta_1 = 0.9$ GHz and $\delta_2 = 6$ MHz. (B) Same as A but at $\delta_1 = 0.5$ GHz and $\delta_2 = -10$ MHz. The red arrow indicates that the red dot lines correspond to the axis of “Noise Power”; the yellow arrow indicates that the blue and yellow traces correspond to the axis of “Intensity.”

thermal radiation, added at the detection level (20). In our scheme, the noise is added to the input pump field prior to the FWM, and thus the noise is present throughout the FWM process in all four fields involved, and yet the quantum measurement’s resolution is stable. Note that the improvement of the SNR due to quantum correlations is not universal and is only applicable for certain parameter regimes. In particular, Fig. 2F shows regions of the negative signal (highlighted by the dark blue color), where quantum correlations yield squeezing $S_N < 0$. As has been shown in the two-photon detuning dependence of SN demonstrated in earlier works (31), the region of quantum correlations results in a higher SNR for squeezing measurement, compared to regions of classical correlations $S_N > 0$. Fig. 2F shows a more general dependence with respect to both one- and two-photon detunings. Nevertheless, the correlated measurement is robust against the noise in both quantum (Fig. 4A) and classical (Fig. 4B) regions of parameters.

Discussion

We have carried out multidimensional FWM spectroscopy with squeezed light detection in hot Rb vapor. We find that quantum squeezing measurements provide additional valuable information compared to classical intensity measurements, through higher-order matter correlations. When optical losses

are included, the spectra show different resonance patterns and provide a most valuable probe of the third-order response. A theoretical model provides an adequate microscopic account of the experiments. Our simulations allow to extract the actual model parameters from the AC Stark shift between the peaks corresponding to $\mu, \nu = \pm$. For instance, one can obtain the relative strengths of the dipole moments $|\mu_{e_2g}|/|\mu_{e_1g}| \approx |\mu_{e_1s}|/|\mu_{e_2s}| \approx \sqrt{8}$. This is consistent with the D_1 line $5^2S_{1/2} \rightarrow 5^2P_{1/2}$ π -transitions. Here the dipole moments expressed in multiples of $\langle J = 1/2 | e\mathbf{r} | J' = 1/2 \rangle \approx 2.99ea_0$, where a_0 is Bohr radius, are given by $\mu_{e_1g} = -\mu_{e_2s} = -1/\sqrt{27}$, $\mu_{e_2g} = \mu_{e_1s} = \sqrt{8/27}$. We can further obtain the dephasing rate characterizing the linewidth given by $\gamma_e \sim \gamma_s \approx 10\Gamma \approx 57.5$ MHz, $\gamma_g \approx \Gamma$ (where Γ is the natural linewidth of the D_1 transition). Squeezed light quantum spectroscopy is robust against external noise and yields sub-shot noise signals. Quantum light generated by the FWM process serves as a useful source for quantum spectroscopy and magnetic field sensors (32), complementing spontaneous parametric down-conversion sources. Our results suggest quantum sensing applications with multiphoton correlated light sources with an unprecedented level of microscopic detail beyond classical measurements.

Materials and Methods

Details of the Experiment. A cavity-stabilized Ti:sapphire laser is used. A polarization beam splitter is used to divide the laser into two beams. One beam serves as the pump beam with frequency ω_{pu} which is vertically polarized. The other beam passes through an acousto-optic modulator to get the probe beam at frequency ω_{pr} . The horizontally polarized probe beam is weak (about 20 μ W) and is equally divided into two by a 50/50 beam splitter. These two beams are used to construct a Mach–Zehnder interferometer, which is used to introduce intensity noise to the FWM process. A piezoelectric transducer is placed in the Mach–Zehnder interferometer to introduce intensity noise. The ^{85}Rb vapor cell is 12 mm long and the temperature of the ^{85}Rb vapor cell is stabilized at 113°C. At the center of the vapor cell, the waist of pump beam is about 620 μ m, and the waist of probe beam is about 330 μ m. Combined by a Glan–Laser polarizer, the pump and the probe beams are crossed in the center of the ^{85}Rb vapor cell. The angle between the signal and pump beams is about 7 mrad. The residual pump beam after the FWM process is eliminated by a Glan–Thompson polarizer. The output probe and conjugate beam with frequency $\omega_c = 2\omega_{pu} - \omega_{pr}$ are sent to two silicon photodetectors (D1 and D2, respectively). The detector’s transimpedance gain is 10^5 V/A, and quantum efficiency is 96%. After the output beams are received by the detectors, we can obtain the dc and rf components of the photocurrents. The dc components from the two ports are sent to an oscilloscope to measure the intensity gain of the system. The rf components from the two ports are subtracted from each other by using an rf S and then analyzed with an SA. The SA is set to a 30-kHz-resolution bandwidth and a 300-Hz video bandwidth.

Theoretical Methods. The third-order susceptibility that enters the FWM gain is derived by second-order perturbation theory with respect to probe and conjugate fields, while the pump field is treated nonperturbatively. The corresponding diagrams and details of the derivations are shown in SI Appendix, section S1. The third-order susceptibility has four terms, $\chi_{ia}^{(3)} = \sum_k \sum_{\mu_g, \nu_g, \lambda_g, \mu_s, \nu_s} A_k \tilde{\chi}_k^{(3)} \mu_{\mu_g \nu_g \lambda_g \mu_s \nu_s}$, where A_k are normalization functions that depend on the propagation length inside the sample and other experimental parameters, k runs over the diagrams $k = ia, ib, iia, iib$ shown in SI Appendix, Fig. S1, and μ_m, ν_m , and λ_m indicate the AC Stark-shifted branches of the transition resonances $\mu_g, \mu_s, \nu_g, \nu_s, \lambda_g = \pm$. The first two terms can be written as

$$\tilde{\chi}_{ia}^{(3)} = \sum_{i,j=1}^2 \frac{\mu_{ge_i} \mu_{e_i s}^* \mu_{se_j} \mu_{e_j g} (\omega_{e_i g}^{(\lambda_g)} - i\gamma_e)}{(\Omega_{e_j g}^{(2)} + \gamma_e^2)(\Delta_{ij}^{\mu_g \mu_s} + i\gamma_s)(\Delta_{ij}^{\nu_g \nu_s} + i\gamma_e)},$$

$$\tilde{\chi}_{ib}^{(3)} = \sum_{i,j=1}^2 \frac{\mu_{ge_i} \mu_{e_i s}^* \mu_{se_j} \mu_{e_j g} (\omega_{e_i g}^{(\lambda_g)} - i\gamma_e)}{(\Omega_{e_j g}^{(2)} + \gamma_e^2)(\Delta_{ij}^{\mu_g \mu_s} - i\gamma_s)(\Delta_{ij}^{\nu_g \nu_s} - i\gamma_e)}, \quad [5]$$

where $\Delta_{ij}^{\mu_g \mu_s} = \omega_{pu} - \omega_{pr} + \omega_{e_i g}^{(\mu_g)} - \omega_{e_j s}^{(\mu_s)}$, and $\gamma_l, l = s, e$ are the dephasing rates of the atomic levels. The corresponding expressions for diagrams iia

and *iib* can be obtained by replacing $\omega_{pr} \rightarrow \omega_c$ and $g \leftrightarrow s$. A summary of the resonant structure of the susceptibility is shown in Table 1.

Note that the discrepancy in the linewidth broadening in simulations in Fig. 3 compared to experimental results of Fig. 2 is caused by a simplified model which does not take into account inhomogeneous broadening. The input/output relations for the field operator in the presence of the optical losses accumulated during the propagation after FWM (28) are given by

$$\begin{aligned}\hat{a}_{pr} &\rightarrow \sqrt{\eta_{pr}}\hat{a}_{pr} + \sqrt{1-\eta_{pr}}\hat{\chi}_{pr}, \\ \hat{a}_c &\rightarrow \sqrt{\eta_c}\hat{a}_c + \sqrt{1-\eta_c}\hat{\chi}_c,\end{aligned}\quad [6]$$

where $\eta_r = \cos(|\hat{\chi}_r^{(1)}|)^2$, $r = pr, c$ and the noise operators $\hat{\chi}$ satisfy the standard boson commutation rules $[\hat{\chi}_r, \hat{\chi}_r^\dagger] = 1$. The corresponding susceptibility of the losses due to the spontaneous/stimulated emission is given by

$$\hat{\chi}_r^{(1)} = B_r \sum_{j=1,2} \frac{\mu_{me_j} \mu_{e_j m} \delta_{e_j m}}{2\Omega_{e_j m}^2}, \quad [7]$$

where $m = s$ for $r = pr$ and $m = g$ for $r = c$ and B_r is a normalization function that depends on the propagation length inside the vapor cell and other experimental parameters. In simulations shown in Fig. 3, both A_k and B_r are

used as fitting parameters. Spectra of the noise are shown in *SI Appendix*, Fig. S4.

Data Availability. The data that support the plots within this paper are available at Open Science Framework: <https://osf.io/5kt96/>.

ACKNOWLEDGMENTS. K.D. gratefully acknowledges support from the National Science Foundation of China (Award 11934011), the Zijing Endowed Young Scholar Fund, East China Normal University, and the Overseas Expertise Introduction Project for Discipline Innovation (111 Project, B12024). J.J. gratefully acknowledges support from Innovation Program of Shanghai Municipal Education Commission (Grant 2021-01-07-00-08-E00100), the National Natural Science Foundation of China (Awards 11874155, 91436211, and 11374104), Basic Research Project of Shanghai Science and Technology Commission (Award 20JC1416100), Natural Science Foundation of Shanghai (Award 17ZR1442900), Minhang Leading Talents (Award 201971), Program of Scientific and Technological Innovation of Shanghai (Award 17JC1400401), National Basic Research Program of China (Award 2016YFA0302103), Shanghai Municipal Science and Technology Major Project (2019SHZDZX01), and the 111 Project (B12024). F.S. acknowledges support from the Cluster of Excellence “Advanced Imaging of Matter” of the Deutsche Forschungsgemeinschaft (DFG), EXC 2056, Project 390715994. S.M. gratefully acknowledges the support of the NSF through Grant CHE-1953045.

1. V. Boyer, A. M. Marino, R. C. Pooser, P. D. Lett, Entangled images from four-wave mixing. *Science* **321**, 544–547 (2008).
2. A. M. Marino *et al.*, Delocalized correlations in twin light beams with orbital angular momentum. *Phys. Rev. Lett.* **101**, 093602 (2008).
3. R. C. Pooser, A. M. Marino, V. Boyer, K. M. Jones, P. D. Lett, Low-noise amplification of a continuous-variable quantum state. *Phys. Rev. Lett.* **103**, 010501 (2009).
4. X. Pan *et al.*, Orbital-angular-momentum multiplexed continuous-variable entanglement from four-wave mixing in hot atomic vapor. *Phys. Rev. Lett.* **123**, 070506 (2019).
5. S. Liu, Y. Lou, J. Jing, Interference-induced quantum squeezing enhancement in a two-beam phase-sensitive amplifier. *Phys. Rev. Lett.* **123**, 113602 (2019).
6. K. Zhang *et al.*, Reconfigurable hexapartite entanglement by spatially multiplexed four-wave mixing processes. *Phys. Rev. Lett.* **124**, 090501 (2020).
7. S. Li *et al.*, Deterministic generation of orbital-angular-momentum multiplexed tripartite entanglement. *Phys. Rev. Lett.* **124**, 083605 (2020).
8. S. Liu, Y. Lou, J. Jing, Orbital angular momentum multiplexed deterministic all-optical quantum teleportation. *Nat. Commun.* **11**, 3875 (2020).
9. R. C. Pooser, B. Lawrie, Plasmonic trace sensing below the photon shot noise limit. *ACS Photonics* **3**, 8–13 (2016).
10. J. Jing *et al.*, Experimental demonstration of tripartite entanglement and controlled dense coding for continuous variables. *Phys. Rev. Lett.* **90**, 167903 (2003).
11. R. Horodecki, P. Horodecki, M. Horodecki, K. Horodecki, Quantum entanglement. *Rev. Mod. Phys.* **81**, 865–942 (2009).
12. J.-W. Pan *et al.*, Multiphoton entanglement and interferometry. *Rev. Mod. Phys.* **84**, 777 (2012).
13. S. L. Braunstein, P. van Loock, Quantum information with continuous variables. *Rev. Mod. Phys.* **77**, 513 (2005).
14. S. Mukamel *et al.*, Roadmap on quantum light spectroscopy. *Mol. Opt. Phys.* **53**, 072002 (2020).
15. K. E. Dorfman, F. Schlawin, S. Mukamel, Nonlinear optical signals and spectroscopy with quantum light. *Rev. Mod. Phys.* **88**, 045008 (2016).
16. F. Schlawin, K. E. Dorfman, S. Mukamel, Entangled two-photon absorption spectroscopy. *Acc. Chem. Res.* **51**, 2207–2214 (2018).
17. F. Schlawin, K. E. Dorfman, B. P. Fingerhut, S. Mukamel, Suppression of population transport and control of exciton distributions by entangled photons. *Nat. Commun.* **4**, 1782 (2013).
18. K. E. Dorfman *et al.*, Monitoring spontaneous charge-density fluctuations by single-molecule diffraction of quantum light. *J. Phys. Chem. Lett.* **10**, 768–773 (2019).
19. S. Asban, K. E. Dorfman, S. Mukamel, Quantum phase-sensitive diffraction and imaging using entangled photons. *Proc. Natl. Acad. Sci. U.S.A.* **116**, 11673–11678 (2019).
20. A. Kalachev *et al.*, Biphoton spectroscopy of YAG:Er³⁺ crystal. *Laser Phys. Lett.* **4**, 722 (2007).
21. D. A. Kalashnikov, A. V. Paterova, S. P. Kulik, L. A. Krivitsky, Infrared spectroscopy with visible light. *Nat. Photonics* **10**, 98–101 (2016).
22. R. E. Slusher, L. W. Hollberg, B. Yurke, J. C. Mertz, J. F. Valley, Observation of squeezed states generated by four-wave mixing in an optical cavity. *Phys. Rev. Lett.* **55**, 2409–2412 (1985).
23. C. F. McCormick, V. Boyer, E. Arimondo, P. D. Lett, Strong relative intensity squeezing by four-wave mixing in rubidium vapor. *Opt. Lett.* **32**, 178–180 (2007).
24. A. M. Marino, R. C. Pooser, V. Boyer, P. D. Lett, Tunable delay of Einstein-Podolsky-Rosen entanglement. *Nature* **457**, 859–862 (2009).
25. J. Jing, C. Liu, Z. Zhou, Z. Ou, W. Zhang, Realization of a nonlinear interferometer with parametric amplifiers. *Appl. Phys. Lett.* **99**, 011110 (2011).
26. F. Hudelist *et al.*, Quantum metrology with parametric amplifier-based photon correlation interferometers. *Nat. Commun.* **5**, 3049 (2014).
27. S. Liu, Y. Lou, J. Xin, J. Jing, Quantum enhancement of phase sensitivity for the bright-seeded SU(1,1) interferometer with direct intensity detection. *Phys. Rev. Appl.* **10**, 064046 (2018).
28. M. Jasperse, L. D. Turner, R. E. Scholten, Relative intensity squeezing by four-wave mixing with loss: An analytic model and experimental diagnostic. *Opt. Express* **19**, 3765–3774 (2011).
29. Z. Yang, P. Saurabh, F. Schlawin, S. Mukamel, K. E. Dorfman, Multidimensional four-wave-mixing spectroscopy with squeezed light. *Appl. Phys. Lett.* **116**, 244001 (2020).
30. K. Dorfman *et al.*, Multidimensional four-wave-mixing signals detected by quantum squeezed-light. Open Science Framework database. <https://osf.io/5kt96/>. Deposited 10 June 2021.
31. Z. Qin, L. Cao, J. Jing, Experimental characterization of quantum correlated triple beams generated by cascaded four-wave mixing processes. *Appl. Phys. Lett.* **106**, 211104 (2015).
32. J. A. Jones *et al.*, Magnetic field sensing beyond the standard quantum limit using 10-spin NOON states. *Science* **324**, 1166–1168 (2009).

Supplementary Information for

Multidimensional four-wave mixing signals detected by quantum squeezed-light

Konstantin Dorfman^{a,1,2}, Shengshuai Liu^{a,1}, Yanbo Lou^{a,1}, Tianxiang Wei^a, Jietai Jing^{a,b,c,d,2}, Frank Schlawin^e, and Shaul Mukamel^f

² Konstantin Dorfman E-mail: dorfman@lps.ecnu.edu.cn;

² Jietai Jing E-mail: jtjing@phy.ecnu.edu.cn

This PDF file includes:

Supplementary text
Figs. S1 to S4

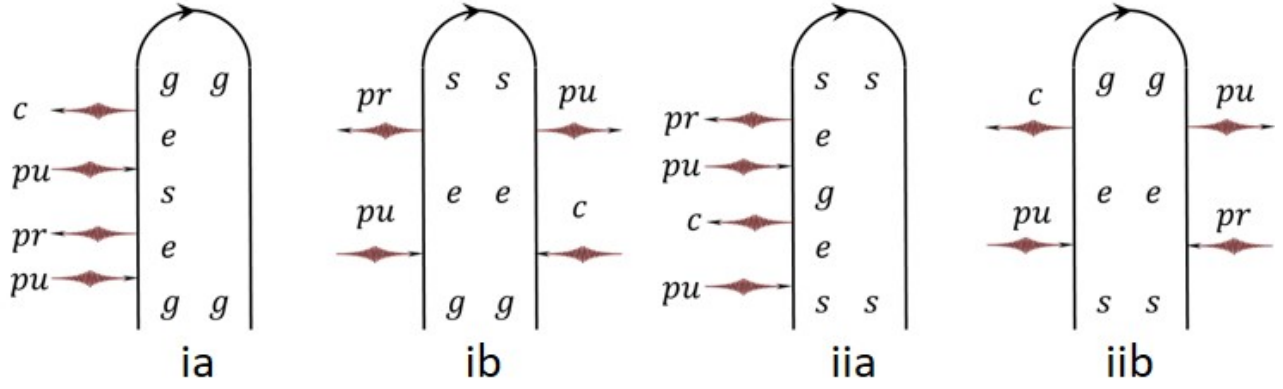


Fig. S1. Diagrams representing the third order susceptibility for the level scheme in Fig. 1b.

Supporting Information Text

S1. Perturbative treatment of weak fields

The field/matter interaction Hamiltonian is

$$H_{FWM} = \int d\mathbf{r} \mu_{eg}(E_c(t, \mathbf{r}) + E_{pu}(t, \mathbf{r})) + \mu_{es}E_{pr}(t, \mathbf{r}), \quad [S1]$$

where the classical pump field $E_{pu}(t, \mathbf{r}) = \mathcal{E}_{pu}e^{-i\omega_{pu}t + i\mathbf{k}_{pu}\cdot\mathbf{r}}$ and the probe and conjugate are quantum fields given by

$$E_j(t, \mathbf{r}) = \sqrt{\frac{2\pi\hbar\omega_j}{V}}(\hat{a}_j e^{-i\omega_j t + i\mathbf{k}_j\cdot\mathbf{r}} + \hat{a}_j^\dagger e^{i\omega_j t - i\mathbf{k}_j\cdot\mathbf{r}}), \quad j = pr, c \quad [S2]$$

We use classical fields to calculate susceptibility components in Eqs. (S11)- (S12), while the quantum nature of the fields is utilized for input-output relations in Eqs. (S13) - (S14) which lead to Eqs. (1) - (2) of the main text. The applicability of classical fields to calculate susceptibility components is a standard procedure. Some discrepancies in susceptibilities at single photon level may be observed, which is not the case for many-photon squeezed light. Lowering and raising operators commonly used with dipole interaction Hamiltonian and two- and three-level quantum system also apply in this case. We thus replace the operators of the probe and conjugate fields by their respective expectation values: $\mathcal{E}_{pr} = \sqrt{\frac{2\pi\hbar\omega_{pr}}{V}}\langle\hat{a}_{pr}\rangle$ and $\mathcal{E}_c = \sqrt{\frac{2\pi\hbar\omega_c}{V}}\langle\hat{a}_c\rangle$. The third-order perturbative approach is visualized by the loop diagrams shown in Fig. S1. In diagrams *ia* and *ib* the initial state is the ground state *g*, whereas in diagrams *iia* and *iib* *s* is the initial state. At high temperatures both *g* and *s* state are almost equally populated. The Schrodinger equation for the state amplitudes

$$|\psi(t)\rangle = [c_g(t)|g\rangle + c_s(t)|s\rangle]e^{i(\omega_{pu}-\omega_e)t} + c_e(t)e^{-i\omega_e t}|e\rangle \quad [S3]$$

is given by

$$\begin{aligned} \dot{c}_g &= -i\delta_{eg}c_g - i\Omega_{eg}^*c_e - i\Omega_c^*e^{i(\omega_c-\omega_{pu})t}c_e, \\ \dot{c}_s &= -i\delta_{es}c_s - i\Omega_{es}^*c_e - i\Omega_{pr}^*e^{i(\omega_{pr}-\omega_{pu})t}c_e, \\ \dot{c}_e &= -i\Omega_{eg}c_g - i\Omega_{es}c_s - i\Omega_c e^{-i(\omega_c-\omega_{pu})t}c_g - i\Omega_{pr}e^{-i(\omega_{pr}-\omega_{pu})t}c_s, \end{aligned} \quad [S4]$$

where $\delta_{em} = \omega_{pu} - \omega_{em}$, $m = g, s$, $\Omega_c = \mu_{eg}\mathcal{E}_c$, $\Omega_{pr} = \mu_{es}\mathcal{E}_{pr}$, and for brevity we omitted the subscript of the *e* state in detunings δ_{em} and Rabi frequencies Ω_{em} treating e_1 and e_2 in a similar fashion. Initial conditions for Eq. (S4) are $c_g(t_0) = 1$, $c_e(t_0) = c_s(t_0) = 0$ for *ia*, *ib* diagrams and $c_s(t_0) = 1$, $c_g(t_0) = c_e(t_0) = 0$ for *iia*, *iib* diagrams. Instead of simply reading the signal from the diagrams in Fig. S1 we deliberately indicate some important steps which will be further used in the strong pump case. We focus on diagram *ia*. Other diagrams can be treated similarly. To derive third order susceptibility we define a signal first, which according to the diagram *ia* is given as a transmission of the conjugate beam:

$$S_{ia}(t) = \text{Im}[\mathcal{E}_c^*(t)P_{ia}^{(3)}(t)], \quad [S5]$$

where third order polarization is given by

$$P_{ia}^{(3)}(t) = \mu_{eg}c_e^{(3)}(t)c_g^{(0)*}(t). \quad [S6]$$

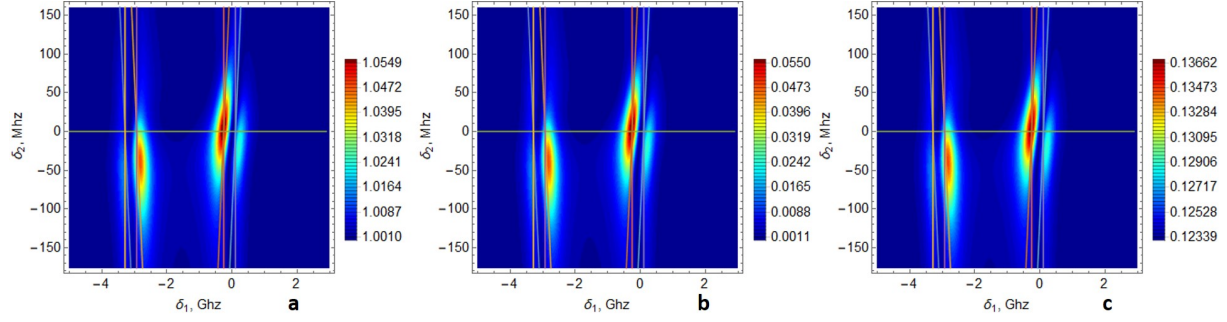


Fig. S2. Calculated perturbative 2D spectra of the probe Eq. (1) with gain governed by perturbative susceptibilities given by Eqs. (S11) - (S12) displayed vs one - δ_1 and two-photon δ_2 detunings - (a), conjugate - (b) and squeezing - (c).

For the weak pump field perturbative orders are taken for all three fields: pump, probe and conjugate. Zeroth order term $c_g^{(0)}(t) = e^{-i\delta_{eg}(t-t_0)}$. Third order amplitude $c_e^{(3)}$ can be calculated in a sequence of 3 steps according to field-matter interactions in diagram ia:

$$c_e^{(3)}(t) = -i\delta_{es} \int_{t_0}^t dt' c_s^{(2)}(t'), \quad [S7]$$

where

$$c_s^{(2)}(t') = -i\Omega_{pr}^* \int_{t_0}^{t'} dt'' e^{i(\omega_{pr}-\omega_{pu})t''} c_e^{(1)}(t''), \quad [S8]$$

where

$$c_e^{(1)}(t'') = -i\Omega_{eg} \int_{t_0}^{t''} dt''' c_g^{(0)}(t'''). \quad [S9]$$

Solving Eqs. (S7) - (S9) and taking the limit $t_0 \rightarrow -\infty$ we obtain

$$P_{ia}^{(3)}(t) = \chi_{ia}^{(3)}(-\omega_{pr}, -\omega_c; 2\omega_{pu}) \mathcal{E}_{pu} \mathcal{E}_{pr}^* e^{-i(2\omega_{pu}-\omega_{pr})t} \quad [S10]$$

where

$$\chi_{ia}^{(3)}(-\omega_{pr}, -\omega_c; 2\omega_{pu}) = \sum_e \frac{|\mu_{eg}|^2 |\mu_{es}|^2}{(2\omega_{pu} - \omega_{pr} - \omega_{eg} + i\gamma_e)(\omega_{pu} - \omega_{pr} - \omega_s + i\gamma_{sg})(\omega_{pu} - \omega_{eg} + i\gamma_e)}. \quad [S11]$$

Similarly we obtain for other diagrams:

$$\begin{aligned} \chi_{ib}^{(3)}(-\omega_{pr}, -\omega_c; 2\omega_{pu}) &= \sum_e \frac{|\mu_{eg}|^2 |\mu_{es}|^2}{(\omega_c - \omega_{eg} - i\gamma_e)(\omega_c - \omega_{pu} - \omega_{sg} - i\gamma_s)(\omega_{pu} - \omega_{eg} + i\gamma_e)}, \\ \chi_{iaa}^{(3)}(-\omega_{pr}, -\omega_c; 2\omega_{pu}) &= \sum_e \frac{|\mu_{eg}|^2 |\mu_{es}|^2}{(2\omega_{pu} - \omega_c - \omega_{es} + i\gamma_e)(\omega_{pu} - \omega_c - \omega_{gs} + i\gamma_s)(\omega_{pu} - \omega_{es} + i\gamma_e)}, \\ \chi_{iib}^{(3)}(-\omega_{pr}, -\omega_c; 2\omega_{pu}) &= \sum_e \frac{|\mu_{eg}|^2 |\mu_{es}|^2}{(\omega_{pr} - \omega_{es} - i\gamma_e)(\omega_{pr} - \omega_{pu} - \omega_{gs} - i\gamma_s)(\omega_{pu} - \omega_{es} + i\gamma_e)}, \end{aligned} \quad [S12]$$

where dephasing rates have been added phenomenologically. The total susceptibility thus is given by $\chi^{(3)} = \sum_k A_k \tilde{\chi}_k^{(3)}$, where A_k are normalization functions that depend on the propagation length inside the sample and other experimental parameters, k runs over the diagrams $k = ia, ib, iia, iib$. Note, that we included normalization constant into the susceptibility itself, for brevity. The quantum state of light generated via FWM is given by $|\psi_{FWM}\rangle = U|\psi\rangle_0$ where $|\psi\rangle_0$ is the incoming state of light before the FWM. The unitary evolution operator $U = \exp(\chi^{(3)} \hat{a}_{pr}^\dagger \hat{a}_c^\dagger / 2 - h.c.)$, where we utilized the quantum nature of the probe and conjugate fields by bringing back their original operator form.

The corresponding input-output relation is given by

$$\hat{a}_{pr} = U^\dagger \hat{a}_{pr0} U = \cosh(s) \hat{a}_{pr0} + e^{i\theta} \sinh(s) \hat{a}_{c0}^\dagger, \quad [S13]$$

$$\hat{a}_c^\dagger = U^\dagger \hat{a}_{c0}^\dagger U = e^{-i\theta} \sinh(s) \hat{a}_{pr0} + \cosh(s) \hat{a}_{c0}^\dagger, \quad [S14]$$

where $s = |\chi^{(3)}|$. The corresponding photon number of the probe, conjugate, and noise figure are given by Eqs. (1) - (2) of the main text and depicted in Fig. S2a, b, and c, respectively. The 2D spectrograms indicate four peaks equivalent to $\delta_1 = 0$, $\delta_1 = -\omega_s$, and $\delta_2 = 0$. There are no Stark shifts associated with the strong field observed in experiment. We notice, that the probe gain is of the order of 1 which results in the absence of amplification and low (10^{-2}) level of the conjugate gain. The corresponding squeezing is also small and positive (classical). It is therefore clear, that stronger pump is required to observe high gain and low noise figure.

S2. Strong pump

When the pump is strong, perturbation theory can be only applied to the probe and conjugate fields. In this case, nonlinear polarization is given by

$$P_{ia}^{(3)}(t) = \mu_{eg} c_e^{(1)}(t) c_g^{(0)*}(t), \quad [\text{S15}]$$

where zeroth order amplitude $c_g^{(0)}$ satisfy the following system of equations:

$$\begin{aligned} \dot{c}_g^{(0)} &= -i\delta_{eg} c_g^{(0)} - i\Omega_{eg}^* c_e^{(0)}, \\ \dot{c}_e^{(0)} &= -i\Omega_{eg} c_g^{(0)} \end{aligned} \quad [\text{S16}]$$

Here we make one important ansatz. Since the AC Stark shift due to the strong pulse affects mostly two peaks 2 and 3 (see Fig. 2), we treat pump-driven transitions $g - e$ and $s - e$ separately. This allows to consider closed two sets of equations involving a pair of amplitudes only. As our results indicate, this ansatz allows to obtain reasonable agreement between peak positions. In this case, solution of Eq. (S16) reads

$$c_g^{(0)}(t) = e^{-\frac{1}{2}\delta_{eg}(t-t_0)} \left[\cos \Omega'_{eg}(t-t_0) - i \frac{\delta_{eg}}{2\Omega'_{eg}} \sin \Omega'_{eg}(t-t_0) \right], \quad [\text{S17}]$$

where $\Omega'_{eg} = \sqrt{\delta_{eg}^2/4 + \Omega_{eg}^2}$ and we assume real Rabi frequency $\Omega_{eg}^* = \Omega_{eg}$. Note, that the standard Rabi oscillations given by Eq. (S17) occur with both Stark shifted energies $\omega_{eg}^{(\pm)} = \delta_{eg}/2 \pm \Omega'_{eg}$. The corresponding $c_e^{(0)}$ amplitude is given by

$$c_e^{(0)} = \frac{\Omega_{eg}}{2\Omega'_{eg}} \left(e^{-i\omega_{eg}^{(+)}(t-t_0)} - e^{-i\omega_{eg}^{(-)}(t-t_0)} \right). \quad [\text{S18}]$$

The solution for the first order amplitude $c_e^{(1)}$ satisfies the following

$$\begin{aligned} \dot{c}_s^{(1)} &= -i\delta_{es} c_s^{(1)} - i\Omega_{es}^* c_e^{(1)} - i\Omega_{pr}^* e^{i(\omega_{pr} - \omega_{pu})t} c_e^{(0)}, \\ \dot{c}_e^{(1)} &= -i\Omega_{es} c_s^{(1)}. \end{aligned} \quad [\text{S19}]$$

Eq. (S19) can be solved exactly analytically. After a bit of algebra one can collect all the necessary terms and obtain an expression for the susceptibility ia and similarly for ib given by Eq. (3).

S3. Optical losses

Similar to the weak pump case, one can account for the optical losses associated with the elastic scattering of the pump into the photon with probe and conjugate frequencies. We define the optical loss coefficient in terms of the linear susceptibility:

$$\eta_r = \cos(|\tilde{\chi}_r^{(1)}|)^2, r = pr, c, \quad [\text{S20}]$$

where $\tilde{\chi}_r^{(1)}$ originate from the linear polarization:

$$P_c^{(1)}(t) = \mu_{eg} c_e^{(0)}(t) c_g^{(0)*}(t) \quad [\text{S21}]$$

Using Eq. (S17) and Eq. (S18) one obtains expression for $\tilde{\chi}_c^{(1)}(-\omega_c; \omega_{pu})$ given by Eq. (5). Similarly one can obtain $\tilde{\chi}_{pr}^{(1)}(-\omega_{pr}; \omega_{pu})$. The importance of the optical losses in experiment can be visualized if one would take a straightforward approach and plot the noise spectra in the absence of the optical losses in Eq. (2) using the data of Fig. 2d. The result shown in Fig. S3 indicates that there is no new information about the system. Rather noise spectra shown in Fig. S3 repeats Fig. 2d with a slightly different scaling. In contrast, real experimental data of the noise figure in Fig. 2f indicates new information accessible only in the presence of the optical losses.

S4. Coefficient of determination

We have calculated the coefficient of determination (R^2) defined as

$$R^2 = 1 - \frac{\sum_i (y_i - f_i)^2}{\sum_i (y_i - \bar{y})^2}, \quad [\text{S22}]$$

where y_i is the experimental value (black dots in Fig. 3), $i=1, \dots, N$. N is the number of the experimental values. \bar{y} is the mean value of experimental values. f_i is the corresponding theory value of y_i (red line in Fig. 3). Based on Eq. (S22), the values of the coefficient of determination (R^2) in Fig. 3b, c, d, f, g, h are 0.41, 0.92, 0.72, 0.85, 0.58, 0.51, respectively. We added the corresponding values in the caption of Fig. 3.

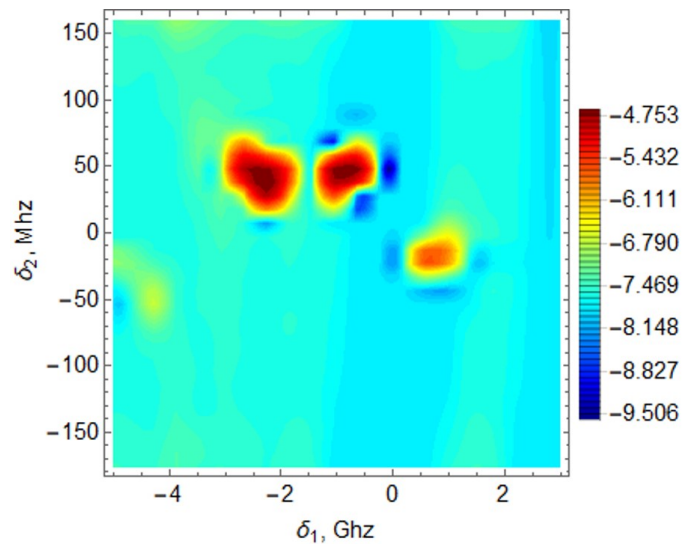


Fig. S3. Noise figure Eq. (2) in the absence of the optical losses for the gain G taken from Fig. 2d.

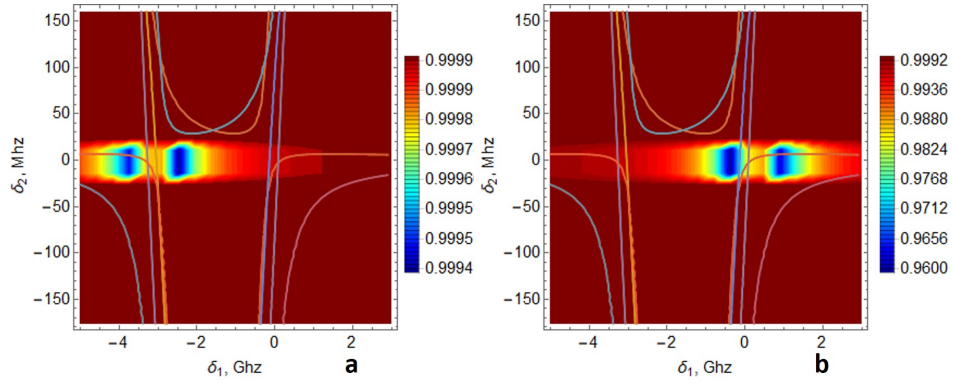


Fig. S4. 2D Spectra Eq. (S20) of the optical losses for the probe η_{pr} and conjugate η_c beams with susceptibilities given by Eq. (5).